Combustion and Flame 246 (2022) 112384

Contents lists available at ScienceDirect

Combustion and Flame

journal homepage: www.elsevier.com/locate/combustflame

Combined experimental and numerical studies on soot characteristics of diesel sprays with split injection strategies

Tiemin Xuan[a], Noud Maes[b], José M. García-Oliver[c,*], Daiana De León-Ceriani[c], Leonardo Pachano[c,1], Zhixia He[d]

[a] School of Energy and Power Engineering, Jiangsu University, Zhenjiang 212013, China
[b] Department of Mechanical Engineering, Eindhoven University of Technology, P.O. Box 513, 5600 MB Eindhoven, the Netherlands
[c] CMT-Motores Térmicos. Universitat Politècnica de València, Valencia 46022, Spain
[d] Institute for Energy Research, Jiangsu University, Zhenjiang 212013, China

ARTICLE INFO

Article history:
Received 22 October 2021
Revised 2 September 2022
Accepted 13 September 2022

Keywords:
Spray A
Soot
Split-injection
Dodecane
Flamelet model
Engine combustion network

ABSTRACT

Experimental and numerical studies on the soot characteristics of Spray A flames were conducted with a focus on the effects of different split injection strategies in high-pressure high-temperature vessels within the engine combustion network. Three high-speed imaging techniques were used to obtain the transient information of flame evolution. Schlieren was applied to identify the spray boundaries and spray penetration. Moreover, a combined extinction and radiation technique was applied to quantify the spatial soot and temperature fields simultaneously. Finally, high-speed OH* chemiluminescence was applied at the baseline condition to measure the temporal high-temperature flame evolution. To substantiate the analysis, the experimental results were compared with the computational fluid dynamics (CFD) predictions from a Reynolds-averaged Navier Stokes approach with Unsteady Flamelet Progress Variable combustion and a two-equation soot-in-flamelet models, which qualitatively reproduced the experimental results.

According to the chosen split injection strategy, dwell and first-injection pulse durations were varied. For all cases, the ignition delay (ID) and soot production of the second-injection pulse were shorter and higher than those of the first one, respectively. A slight change in the experimental soot production was observed when the dwell time was changed. The CFD calculations revealed a small reduction in the ID of the second pulse with long dwell times, which was due to variations in the interaction between the newly injected fuel and combustion recession. However, the effect of dwell variation was extremely small to produce significant differences in the evolution of the second pulse, neither in combustion nor in soot production. With regard to the duration of the first injection, no effect on the experimental soot production of the second pulse was observed despite noticeable differences due to the first pulse. The CFD results indicated that because of the quasi-steady flow and combustion process near the nozzle along the first injection, the evolution of the spray in the region close to the nozzle was identical in all first-pulse-duration cases, with differences only occurring at the tip of the first pulse jet. Thus, the second pulse evolution occurred under identical conditions for ignition and soot production. Although the sensitivity to both dwell and first-pulse durations was low, the CFD analysis highlighted the important effects of both end-of-injection wave propagation and combustion recession on the ignition and soot production of the second pulse.

1. Introduction

As injection equipment have become highly flexible and the role of fuel injection and mixing on the performance of internal combustion engines (ICEs) has been evidenced, understanding the impact of injection strategies has become imperative for the future generation of ultra-clean propulsion systems. Undoubtedly, the use of split injection schemes aimed at reducing engine-out pollutants, such as soot emissions in ICEs, remains relevant. Nevertheless, experimental and numerical studies have shown that the use of biodiesel and its blends with alcohols combined with split injection schemes can significantly reduce soot emissions compared with single injection operation [1–4]. According to a recent

* Corresponding author.
E-mail address: jgarciao@mot.upv.es (J.M. García-Oliver).
[1] Present address: Barcelona Supercomputing Center (BSC), Plaça Eusebi Güell 1–3, Barcelona 08034, Spain

https://doi.org/10.1016/j.combustflame.2022.112384

Nomenclature

ICEs	internal combustion engines
DNS	direct numerical simulation
ASOI1	after start of first injection
ASOI2	after start of second injection
CER	combined extinction and radiation
CFD	computational fluid dynamics
ECN	engine combustion network
IDi	ignition delay, i = 1,2 correspond to first/second injection pulse
LOLi	lift-off length, i = 1,2 correspond to first/second injection pulse
LES	large-eddy simulation
RDG	Rayleigh-Debye-Gans
TCI	turbulence chemistry interaction
TDC	top dead center
UFPV	unsteady flamelet/progress variable
$L_{\nabla \mathrm{Mdot}_{\max}}$	distance to the nozzle of the position of the maximum axial gradient of momentum flux
m_{soot}	total soot mass as a function of time.
Yc	progress variable

experimental study on a four-cylinder compression ignition engine characterizing engine-out soot emissions, the split injection scheme induces distinct changes in the physicochemical characteristics of soot particles, which are partly responsible for the reduction in soot production [5]. Previous studies on optical engines [6–8] have presented clear evidence regarding how the interaction of soot structures in the main injection and post injection reduced soot production compared with that in single-injection operation.

Similar to many complex processes, investigations under simplified conditions aid in decoupling interactions that may obscure the underlying physics. In this context, the study of split injections in dedicated optically accessible combustion vessels is useful as it isolates the phenomena to be examined. In these combustion vessels, sprays are evaluated in a quiescent environment without moving parts under well-characterized ambient conditions. Considerable progress has been achieved in understanding the mechanisms behind the spray–spray interaction, mixing, and combustion in split injection schemes in quiescent environments. Evidence of how the second injection is characterized by faster spray tip penetration compared to the first pulse (resulting from the combination of the slipstream effect [9] and lower local density induced by the combustion recession of the first injection) has been consistently reported in experimental [9,10] and numerical studies [11–13]. Combustion recession has also been reported to reduce the ignition delay (ID) of the second injection owing to the presence of hot remnants from the first injection. In the study of split injection schemes, the appearance of an entrainment wave [14] has been reported and supported by direct numerical simulation (DNS) results [15,16]. Recently, DNS results also showed that, unlike the first injection, which is characterized by auto-ignition, the ignition of the second injection is more representative of a premixed combustion event driven by diffusion in the flame-tangential direction [17]. In terms of soot production, experimental [18,19] and numerical studies [20,21] indicate that the earlier ignition of the second injection and its stabilization at fuel-rich locations near the nozzle compared to the first one cause increased soot production [21]. In contrast, the oxidation of soot from the first injection is enhanced by the second injection event because more oxygen is entrained into the first injection soot region [18].

The investigation of the parameters controlling the interaction among injection pulses (e.g., first-injection duration and dwell time) was beyond the scope of the aforementioned studies. In this sense, the mixing process and ignition event have been experimentally [22] and numerically [23,24] characterized by the changes in dwell time. Bruneaux and Maligne [22] reported a faster mixing of the second injection with a shorter dwell time because of the more intense interaction among the velocity fields. For the ignition event, the reported trends depended on the length of the dwell time under study. With relatively short dwell times (in the order of 0.875 *ms*), the decrease in the ID of the second injection is attributed to the interaction with CH_2O remnants from the first injection [22]. In contrast, with relatively long dwell times (in the order of 1.75 *ms*), the ignition of the second injection is delayed [23–25]. Zhao et al. [24] showed that as the dwell time increased, fewer intermediate products (favoring ignition) and more final products of combustion (inhibiting ignition) are left along the path of the second injection, leading to an increase in the ID. Additionally, the interaction between the two injections was delayed with longer dwell because the time required for the second injection to reach the tail of the first injection was longer.

Few studies have focused on the effect of dwell time on soot production. Brands et al. [25] reported natural luminosity results for dwell times of 0.75 and 1.25 *ms*. A trend could not be established because the amount of soot was not quantified. Moiz et al. [26] conducted large-eddy simulations and reported that the observed decrease in soot mass due to longer dwell times (from 0.5 to 0.65 *ms*) might be attributed to the increased air entrainment resulting from the second injection stabilizing further downstream. Nonetheless, no experimental data were available for validation.

Within this context, the main objective of this study is to characterize the role of dwell time and first-injection duration on the soot production in split injection schemes and to identify the mechanisms behind the observed trends. Similar to many of the preceding works, the baseline condition is the Engine Combustion Network (ECN) Spray A standard case with a 0.5-*ms* first injection, 0.5-*ms* dwell time, and 0.5-*ms* second injection. Parametric variations around this operating condition comprise four additional conditions to study the roles of the dwell time (0.3 and 0.7 *ms*) and first-injection duration (0.3 and 0.7 *ms*). The characterization of combustion and soot production relies on high-speed schlieren, combined extinction and radiation methodology (CER) [27], and OH* chemiluminescence measurements.

Although experimental measurements were first reported in [28], the results and trends discussed in this paper are supplemented by the CFD predictions from the Unsteady Flamelet Progress Variable (UFPV) model that has been extended to account for the soot production with a soot-in-flamelet model [29]. To the best of the authors' knowledge, this is the first time that (1) soot production is characterized based on the simultaneous experimental quantification of the soot amount and temperature for different dwell times and first injection duration. Moreover, (2) soot production trends are linked to the end-of-injection wave propagation, as quantified from the CFD momentum flux distribution.

2. Experimental methodology

2.1. High-pressure high-temperature vessels

Measurements were conducted in two different high-pressure high-temperature vessels capable of reproducing the thermal conditions at the top dead center position of diesel engines. In this study, high-speed schlieren imaging and soot visualization were performed in a constant-pressure vessel at CMT-Motores Térmicos (CMT). High-speed OH* chemiluminescence data were obtained from a constant-volume vessel at the Eindhoven University of Technology (TU/e). Two single-hole Spray A injectors (nominal diameter d_0 = 90 μm), identified as #210675 (CMT) and #306.22

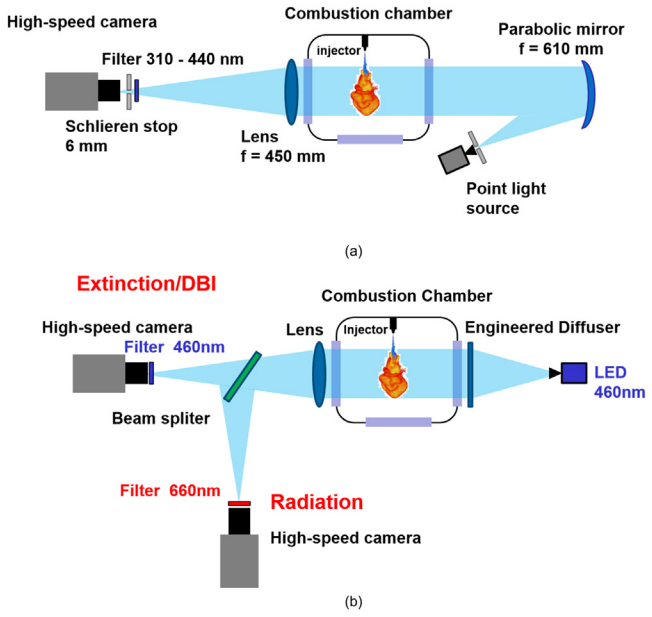

Fig. 1. Schematics of (a) high-speed schlieren imaging and (b) CER setup.

(TU/e), had been characterized in previous studies [30,31]. Detailed information on these two vessels can be found in various previous publications [10,27,32,33].

2.2. Optical diagnostics

In this study, the high-speed schlieren imaging technique was applied to detect the temporal development of the spray area and quantify the spray tip penetration. Additionally, both ID and lift-off length (LOL) were obtained from schlieren movies based on the analysis of the total intensity increment within the spray between two consecutive images and the analysis of radial expansion, respectively [33,34]. The CER methodology [27] was used to measure the soot extinction and radiation temperature distribution simultaneously. Schematics of the schlieren and CER measurements are shown in Fig. 1. More detailed information on the camera configurations and image-processing methodology of these techniques can be found in previous studies [27]. While schlieren and CER measurements were reported in [28], the transient OH* radical information of the baseline case was also obtained from the high-speed OH* chemiluminescence reported in [10] to complement the soot analysis.

The primary variable measured from the CER extinction images is the optical thickness, KL, which is combined with the radiance images to derive the soot volume fraction (SVF) and temperature on the spray symmetry plane. For this transformation, the soot density is assumed to be $\rho_{soot} = 1.8$ g/cm^3 [35] and the dimensionless extinction coefficient ($k_e = 7.59$) is calculated using the Rayleigh–Debye–Gans (RDG) theory [36]. The parameters used for the RDG approximation were referenced from [37] (fractal prefactor: $k_f = 8.36$; fractal dimension: $D_f = 1.77$; refractive index: $m = 1.75-1.03i$ [38]; aggregate size: $N_p = 150$; particle diameter: $d_p = 16$ nm; and wavelength: $\lambda = 460$ nm). Skeen et al. [39] found that the effect of d_p on k_e is limited when the particles are less than 20 nm; this is based on the transmission electron microscopy measurements of soot from high-pressure spray flames. A time-dependent one-dimensional soot distribution ($m_{soot}(x,t)$) map was obtained by integrating the line-of-sight soot mass along the radial direction. The projected OH* intensity $I_{OH}(x,t)$ maps were similarly obtained. More detailed information regarding the processing procedure is presented in [34].

3. Computational setup

Numerical simulations were performed using the CONVERGE CFD solver [40] and the methodology described in previous publications [29,41]. Here, only the most relevant features are summarized. The domain is a cylinder with a length of 102 mm and radius of 50 mm, reproducing the inner geometry of the high-pressure high-temperature vessel. The base mesh grid was composed of 2-mm cubes. In the near-nozzle area, the grid mesh resolution was refined using truncated cone-shaped fixed embedding. The adaptive mesh refinement capability of CONVERGE based on velocity, temperature, and fuel mass fraction gradients was used to reach a minimum cell size of 125 μm.

Owing to the multiphase nature of the problem, the Lagrangian parcel Eulerian fluid approach was used. The Favre-averaged flow equations were solved within the Reynolds-averaged Navier–Stokes (RANS) framework. Combustion was modeled using a UFPV approach, which is based on the description of a turbulent flame as a set of strained laminar counterflow flamelets. The turbulence–chemistry interaction is considered by assuming that the mixture fraction and scalar dissipation rate are statistically independent using a presumed probability function approach for these two variables.

The chemical mechanism used to describe the n-dodecane oxidation was developed by Narayanaswamy et al. [42] with 255 species and 2289 reactions, including the PAH chemistry required to model the soot precursors. The flamelet code developed at the Argonne National Laboratory [43] was used to generate laminar tables. In this context, a two-equation soot model implemented in [29] was used to quantify the soot production in the studied split injection cases.

4. Test matrix

The operating conditions are summarized in Table 1. The injection pressure ($P_{inj} = 1500$ bar) and thermodynamic conditions (ambient density: 22.8 kg/m^3; ambient temperature: 900 K; and O_2 concentration: 15%) correspond to the standard ECN split injection case. Note that all the injection-relevant times in the present study were defined as the hydraulic injection duration, which was determined by observation from high-speed camera images. Dwell time was defined as the interval between the end of the first injection and the start of the second injection. The operating point in bold is the baseline case (500–500–500), which has been analyzed in depth, as reported in previous publications [9]. This condition is examined in detail here using schlieren/CER/OH* to validate the CFD model. Parametric variations have been investigated by means of CER and schlieren (for some operating conditions). To reduce cycle-to-cycle scattering, 15, 40, and 17 injections were recorded using schlieren imaging, the CER technique, and OH* chemiluminescence, respectively.

All the cases were simulated using CFD calculations. For different cases, the injection rate shapes were generated using the virtual injection rate generator for Spray A available on the CMT website [44].

5. Results and discussions

5.1. Baseline condition

Figure 2 illustrates the time development of the main events for the baseline case based on different spray metrics. Figure 2(a) shows the CFD-derived time-resolved tip penetration and LOL overlaid on the OH field together with the position of the maximum spatial gradient of the momentum flux, $L_{\nabla \mathrm{Mdot}_{max}}$, which is used to track the end-of-injection entrainment wave, as discussed in

Table 1
Matrix with test conditions; operating point in bold is referred to as baseline case.

Operating point	1st Injection [μs]	Dwell [μs]	2nd Injection [μs]	Techniques
500–300–500	500	300	500	CER
500–700–500	500	700	500	Schlieren + CER
500–500–500	**500**	**500**	**500**	**Schlieren + CER + OH***
300–500–500	300	500	500	CER
700–500–500	700	500	500	Schlieren + CER

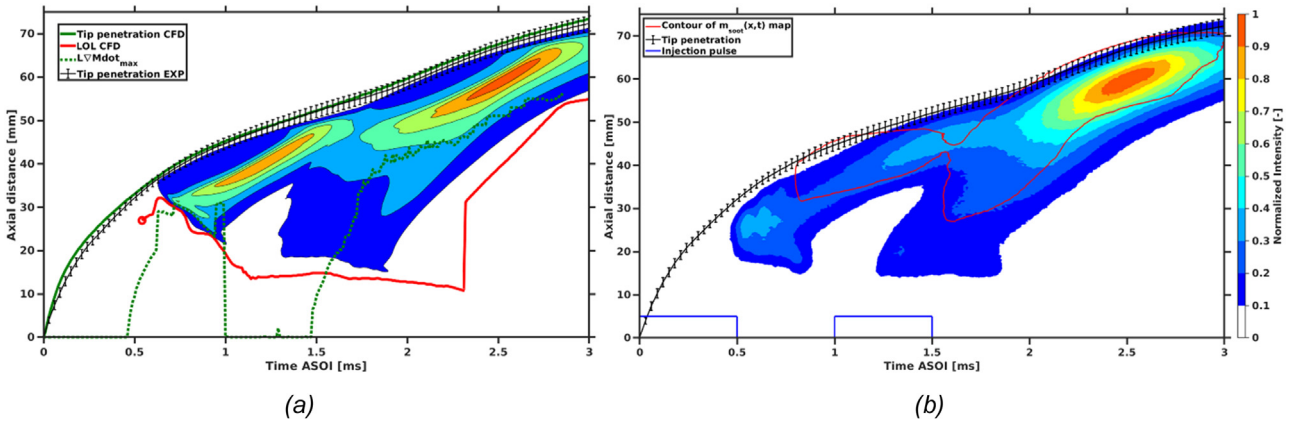

Fig. 2. Spatial and time development of baseline case from (a) CFD and (b) experiments. Tip penetration evolution from both CFD and experiments is repeated on both plots; the latter includes error bars (± 1 standard deviation). (a) For CFD, a contour plot corresponding to the projected OH mass, LOL, and position of maximum momentum flux gradient is included. (b) For experimental cases, a contour plot corresponding to the projected OH* radiation and red contour showing the axial extent where soot is measured are included. Both projected OH mass and OH* radiation have been normalized to the maximum value. A sketch of the injection pulse duration is provided in (b).

Table 2
Nominal condition ID and LOL for both injection pulses obtained by schlieren, OH* chemiluminescence, and numerical CFD simulation.

500–500–500	**ID1 [μs]**	**ID2 [μs]**	**LOL1[mm]**	**LOL2[mm]**
EXP - SCH	$(4.98 \pm 0.25)\cdot10^2$	–	14.3 ± 0.4	11.8 ± 1.5
EXP – OH*	$(4.00 \pm 0.20)\cdot10^2$	$(1.10 \pm 0.20)\cdot10^2$	14.4 ± 1.2	11.0 ± 0.5
CFD	$5.50\cdot10^2$	$1.10\cdot10^2$	30.1	13.0

Appendix B. Figure 2(b) shows the projected OH* map obtained from the experiments overlaid with the spray penetration and a limiting soot mass $m_{soot}(x,t)$ contour. A sketch of the injection pulses is also provided. The tip penetrations from the experiments (farthest location reached by the spray resulting from both injection pulses) and numerical simulation (farthest location on the spray axis where the mixture fraction equals 0.001) are compared in Fig. 2(a). The LOL (from CFD calculations) was defined as the minimum axial distance from the nozzle to the first location where 14% of the maximum OH mass fraction in the domain was reached for every time step. The LOL (from CFD calculations) starts from the ignition of the first pulse, which occurs at 550 μs, according to the computational results (Table 2).

The penetration steadily increases from the start of injection at a rate that varies over the injection period owing to the influence of momentum flux pulses as well as corresponding ignition events. The first pulse is injected into a fundamentally inert atmosphere and the ignition occurs at 550 μs (i.e., at the end of the injection time). The first end-of-injection event coincides with the start of the entrainment wave from the nozzle orifice toward the jet tip, which is tracked based on $L_{\nabla \mathrm{Mdot}_{\max}}$. The previous studies conducted under inert spray conditions [45] indicated that this wave progressed at a velocity approximately twice that of the initial tip penetration. Based on this estimation, it must reach the tip of the jet at approximately 1000 μs (i.e., twice the pulse duration) when a clear deceleration in the overall penetration rate is observed. This estimation considering inert conditions is relatively accurate for the present reacting case where the ignition of the first pulse eventually increases the velocity and accelerates the penetration rate; the foregoing is similar to what has been demonstrated in studies on long injections [27]. In fact, a sudden jump in $L_{\nabla \mathrm{Mdot}_{\max}}$ can be observed at approximately 550 μs (ignition timing); this jump is not caused by a fast wave propagation. To the contrary, the ignition-induced flow rearrangement resulted in a second maximum of the momentum gradient further away from the nozzle. This was more distant than that corresponding to the actual end-of-injection entrainment wave (Fig. 17). After this jump, the maximum gradient of the momentum recedes toward the nozzle (similar to the LOL behavior), confirming that the source of this jump is linked to the combustion-induced change in flow pattern.

The second-injection pulse started at 1000 μs; however, the effect of this second momentum flux pulse on the overall penetration could not be observed until approximately 1700 μs (well beyond the end of injection), as denoted by the clear inflection point from which the rate of penetration increased. Owing to the short ID of the second pulse and the reduced LOL observed both in the CFD and experimental OH* radiation, this second pulse behaves more as a fully reacting jet. The end of this second pulse at 1500 μs created a second end-of-injection wave traveling at a speed similar to that occurring after the end of the first one. This perturbation steadily propagated into the reacting flow with a slight increase in the slope at 1550 μs as it moved past the LOL into the reacting zone. It exhibits a noticeable reduction in slope at 1900 μs and then evolves relatively parallel to the tip penetration. This behavior indicates that using $L_{\nabla \mathrm{Mdot}_{\max}}$ to define the entrainment wave position cannot determine the exact interaction

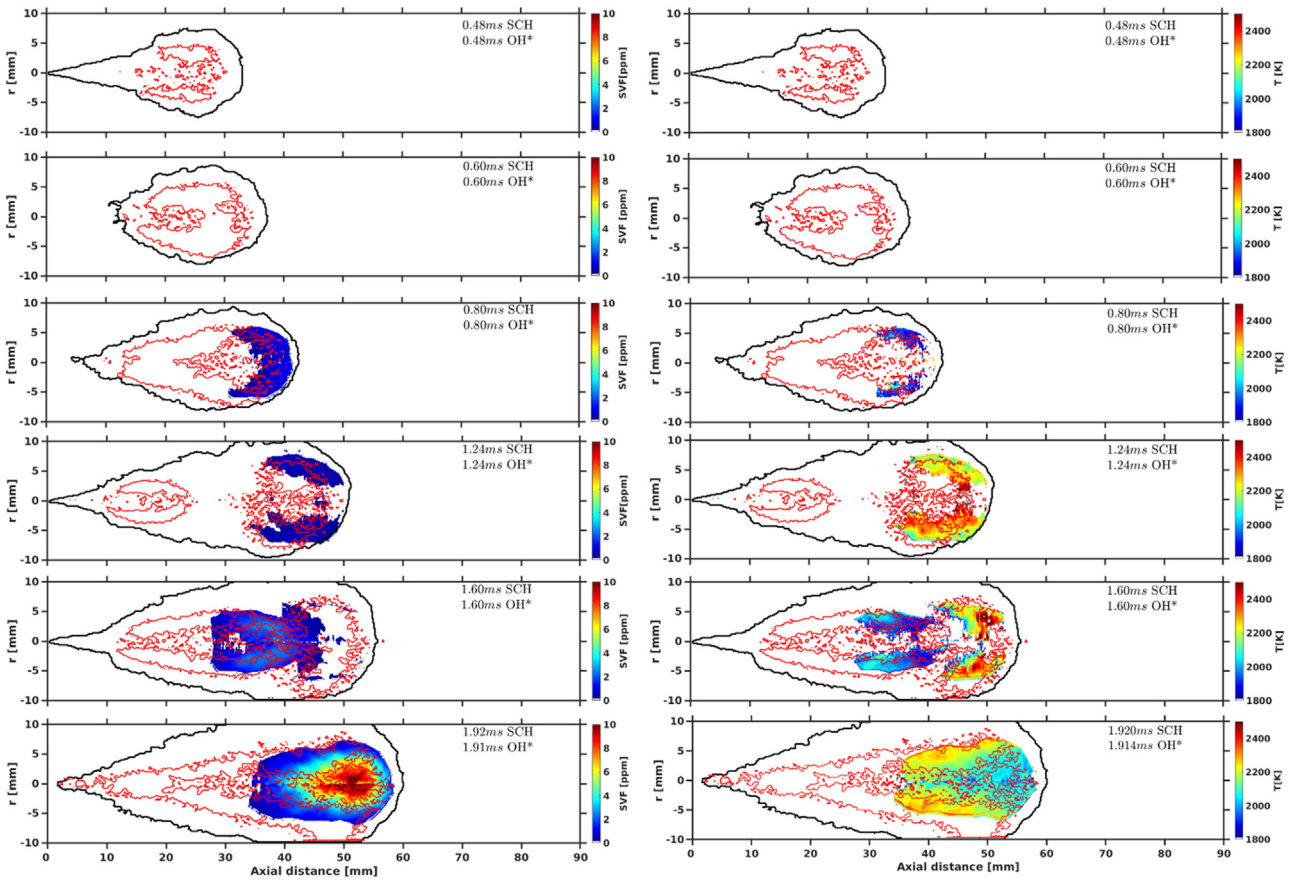

Fig. 3. Reacting spray evolution of baseline case (500–500–500) as derived from experimental information. Black contours represent spray boundaries from schlieren images, whereas red contours represent boundaries on symmetry plane based on OH* images. Contours in color correspond to SVF (left) and temperature (right); time refers to ASOI1.

between the end-of-injection pulse and jet head owing to the presence of the recirculation vortex. Hence, after reaching the tip zone, $L_{\nabla \mathrm{Mdot}_{\max}}$ loses the meaning of the end-of-injection wave and essentially tracks the tip vortex evolution (i.e., the tip penetration behavior). At 2500 μs, the rate of penetration eventually decelerates, indicating that the entrainment wave from the second-injection pulse reaches the tip. Similar to the first pulse injection, this approximately coincides with a time lapse of twice the second pulse duration from the start of the second injection.

The projected OH* map obtained from the experiments shows (starting from the ID of the first pulse) how the observed intensity spreads along the full spray length starting from approximately 15 mm. As the second injection proceeds and ignites, the maximum upstream location of OH* stabilizes at a relatively constant value. Subsequently, a second island of OH* intensity can be observed to proceed downstream starting from an axial distance of 50 mm at 2000 μs and up to 65 mm at 2800 μs (Fig. 2(b)); this is in good agreement with the second end-of-injection wave. Note, however, that the contribution of soot incandescence can interfere with the OH* signal, especially within the locations limited by the soot contour (red line) where a high soot density is obtained [46]. In general, all the three optical techniques show consistent results although they were obtained using different injectors from different test rigs. This supports the conclusions derived from the proposed comparison.

Although CFD data were derived from the ground-state OH species, the overall evolution in terms of the projected OH map is similar to that of the experimental OH* map. The main discrepancy between the simulations and experiments was observed during the ignition of the first pulse, which was delayed in the numerical results. In contrast, all previously described events were appropriately captured starting from 1000 μs. In general, a good correlation between the experimental and CFD results indicates an adequate prediction of flow evolution and overall mixing characteristics consistent with previous results for long injection pulses [29]. Ignition subsequently occurred before (in the experiments) or after (in CFD) the first-injection pulse. This results in an initial LOL evolution that exhibits a highly transient behavior from ignition until approximately 1000 μs with a clear recession toward the orifice. This was considered in the comparison of the average values of the parameter for the first-injection pulse. Table 2 summarizes the global ID and average LOL for the nominal injection case based on schlieren imaging, high-speed OH* chemiluminescence, and CFD predictions. Note that ID1 and LOL1 correspond to the first-injection pulse, and ID2 and LOL2 correspond to the second pulse. The ID derived from schlieren is based on the analysis of the total intensity increment within the spray. The initial spray expansion of the second injection during ignition is difficult to detect because it occurs within the combustion products of the first injection. Hence, only the OH*-derived experimental ID2 was included because the schlieren-based measurement was unreliable.

For both schlieren and OH* chemiluminescence, ID1 is extremely similar to that of the standard long-injection nominal Spray A condition [47] (i.e., virtually coincident with the end of the first injection). The listed values of the experimental and numerical LOLs in the table represent the averages obtained between 500 and 700 μs after the start of injection (ASOI). The results in Fig. 2 show that the LOL during the combustion period of the first pulse is highly transient. Both experimental techniques result in a similar LOL1 in the order of 14 mm. As for the CFD results, both ID1 and LOL1 tended to be overpredicted in line with the previous results with this modeling setup. This is attributed to the chosen chemi-

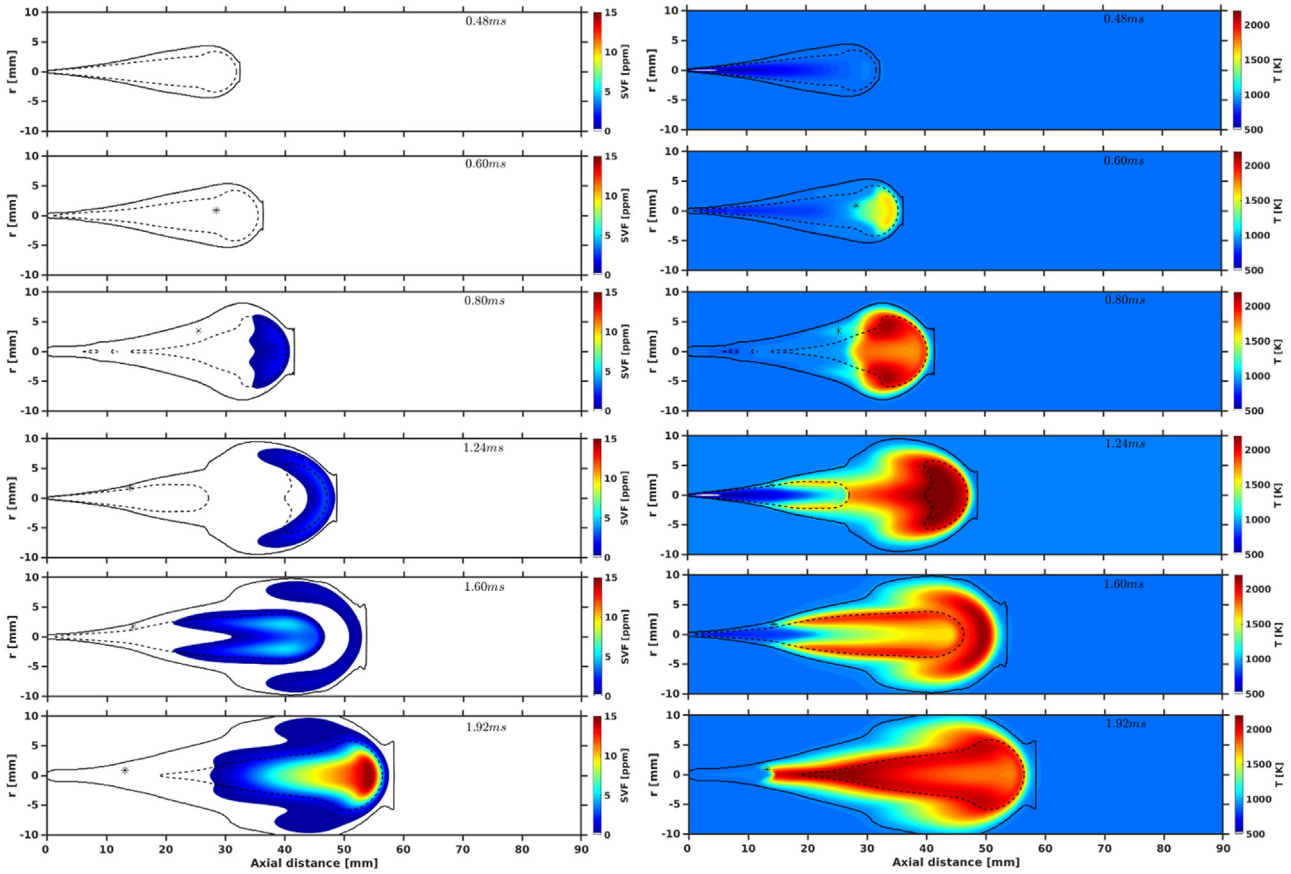

Fig. 4. Reacting spray evolution of baseline case (500–500–500) as derived from CFD calculations. Solid black lines represent spray contour, dashed black lines indicate stoichiometric mixture fraction, and asterisks represent LOL in each panel. Contours in color correspond to SVF (left) and temperature (right); time refers to ASOI1.

cal mechanism [41]. However, ID2 and LOL2 are shorter than those corresponding to the first pulse because of the high-temperature environment created by the first injection resulting in reduced ID2. This is also confirmed by the numerical simulations that are in agreement with the previous results of Skeen et al. [9]. For the second pulse, CFD yielded better predictions for both combustion indicators. This is because ignition occurs in the region where high-temperature combustion products are present. These products can compensate for the deficiencies of the chemical mechanism when predicting the ignition starting from an entirely inert mixture.

As for the soot analysis, a time sequence of the SVF and soot temperature (T) maps on a symmetry plane for the baseline case (500–500–500) based on experimental results are shown in Fig. 3. In addition, experimental spray contours derived from schlieren probability maps [27] (using 50% as a threshold) and contours derived from reconstructed OH* chemiluminescence images on a plane, marked by black and red, respectively, are presented in the figure. Figure 4 shows the CFD results corresponding to the timings shown in Fig. 3. The solid and dashed black lines in the numerical results represent the spray contour and stoichiometric mixture fraction location, respectively; the asterisk indicates the position of the LOL for each time. Time refers to ASOI1 (after the start of the first injection).

- The first timing was 480 μs ASOI1 immediately after the ignition of the first pulse in the experiments where OH* chemiluminescence was clearly observed within the schlieren-derived spray contour at an intermediate radial position from the spray axis to the periphery. At this time, the heat release readily caused the spray to expand from 20 mm until the tip in contrast with the inert situation. This is evident when the experimental schlieren contour is compared with the corresponding CFD one (Fig. 4), which is fully inert because numerical ignition is delayed.
- At 600 μs ASOI1, the first injection had already finished. The entrainment wave [45] (positioned at approximately 20 mm, as shown in Fig. 1) rapidly decreased the mixture fraction in the near-nozzle region after the end of the first injection. This is followed by a combustion recession event toward the nozzle where low-temperature ignition also plays a significant role and softens the dense gradients, which contributes to the rapid disappearance of the schlieren signal [48]. On the numerical side, the maximum temperatures were found at the tip of the jet. No soot was detected during the measurements or calculations.
- At 800 μs ASOI1, the high-temperature phase of combustion recession occurs. With this recession, the LOL moves back toward the injector orifice, as indicated by the schlieren contour. This phenomenon is also observed in the CFD results where the asterisk representing the LOL moves toward the nozzle position (to an extent less than that of the experiments). Meanwhile, soot from the first injection can be observed at the spray head, where both soot quantity and temperature remain relatively low.
- At 1240 μs ASOI1 (or 240 μs ASOI2), the second injection had already undergone ignition, and the corresponding OH* signal from the second pulse was detected. As indicated by Table 2, this occurs earlier than the first ID because of the high-temperature environment and combustion radicals created by the first injection. The soot corresponding to the remnants of the first pulse could only be observed at the tip.

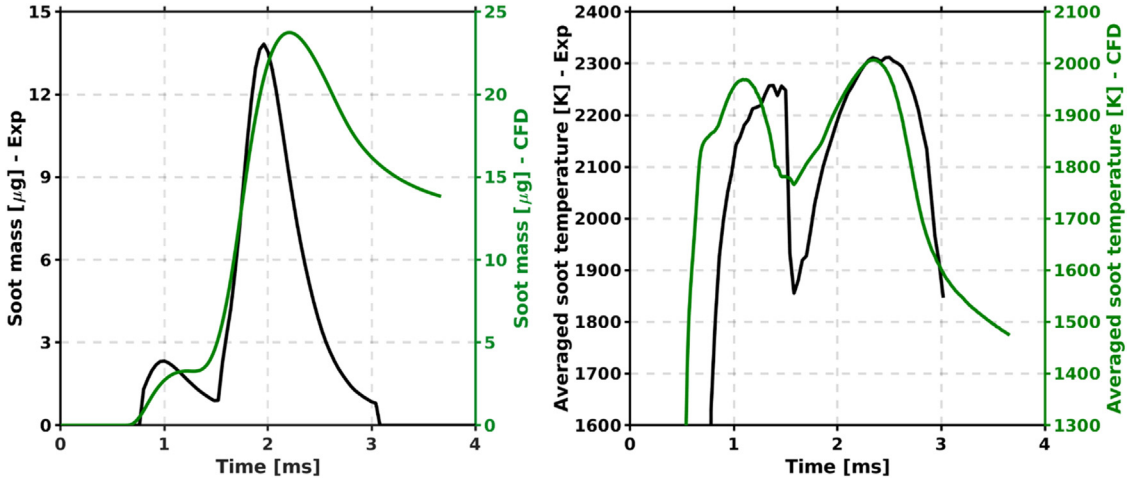

Fig. 5. Temporal evolution of (a) total soot mass and (b) average soot temperature (experiments shown in black and CFD in green) as function of ASOI1 for baseline case. Experimental and numerical values are shown on different y-axis to emphasize qualitative agreement.

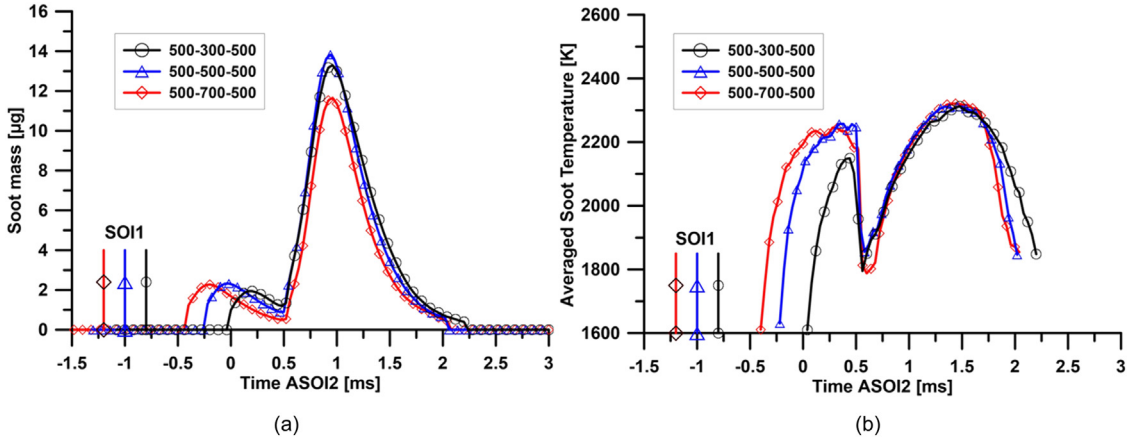

Fig. 6. (a) Temporal evolution of total soot mass and (b) average soot temperature in experiments of different dwell time cases as a function of ASOI2.

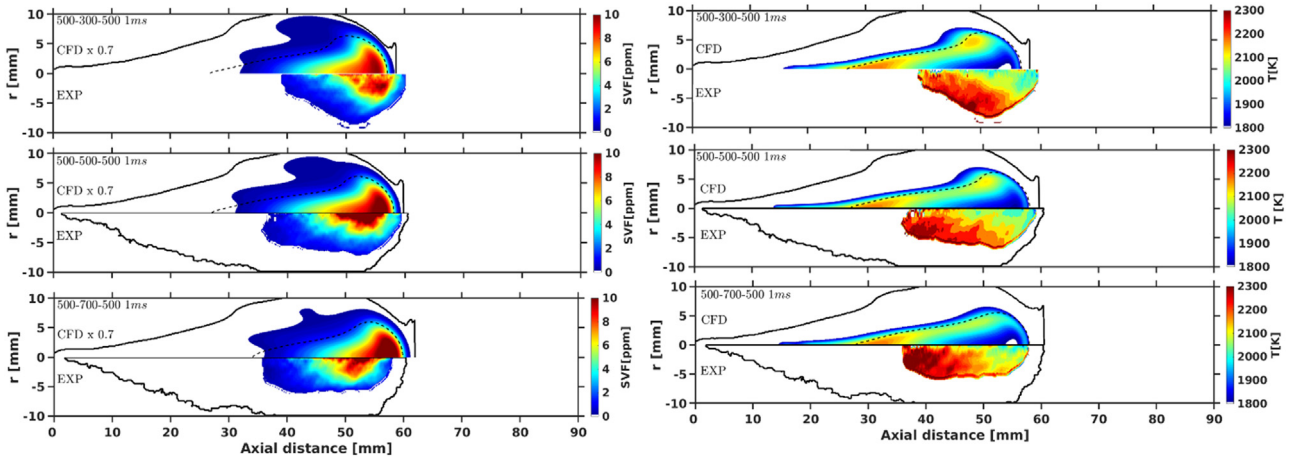

Fig. 7. Experimental (bottom half-plane) and numerical (top half-plane) results of SVF on symmetry plane (left panels) and soot temperature distribution (right panels) at 1000 μs ASOI2 for different dwell time cases: 500–300–500 (top), 500–500–500 (middle), and 500–700–500 (bottom). Black solid lines identify spray boundaries, and dashed lines correspond to stoichiometric surface. To enable comparison between CFD and experimental results with the same color scale, SVF corresponding to CFD is multiplied by 0.7.

- At 1600 μs ASOI1, the second injection was complete, and the corresponding entrainment wave was located at approximately 19 mm (Fig. 2). The soot formed by the second pulse was observed further downstream (30–40 mm in the experiments and 40–50 mm in CFD). This soot cloud moves downstream; however, it does not reach the soot of the first injection, which maintains the highest temperature at the spray head within the contours derived from OH^* chemiluminescence. Calculations show the soot production of the second jet inside the stoichiometric surface. Compared with the first pulse, soot location is closer to the nozzle. As for the temperature maps, the interaction of the high-temperature soot from both injection pulses

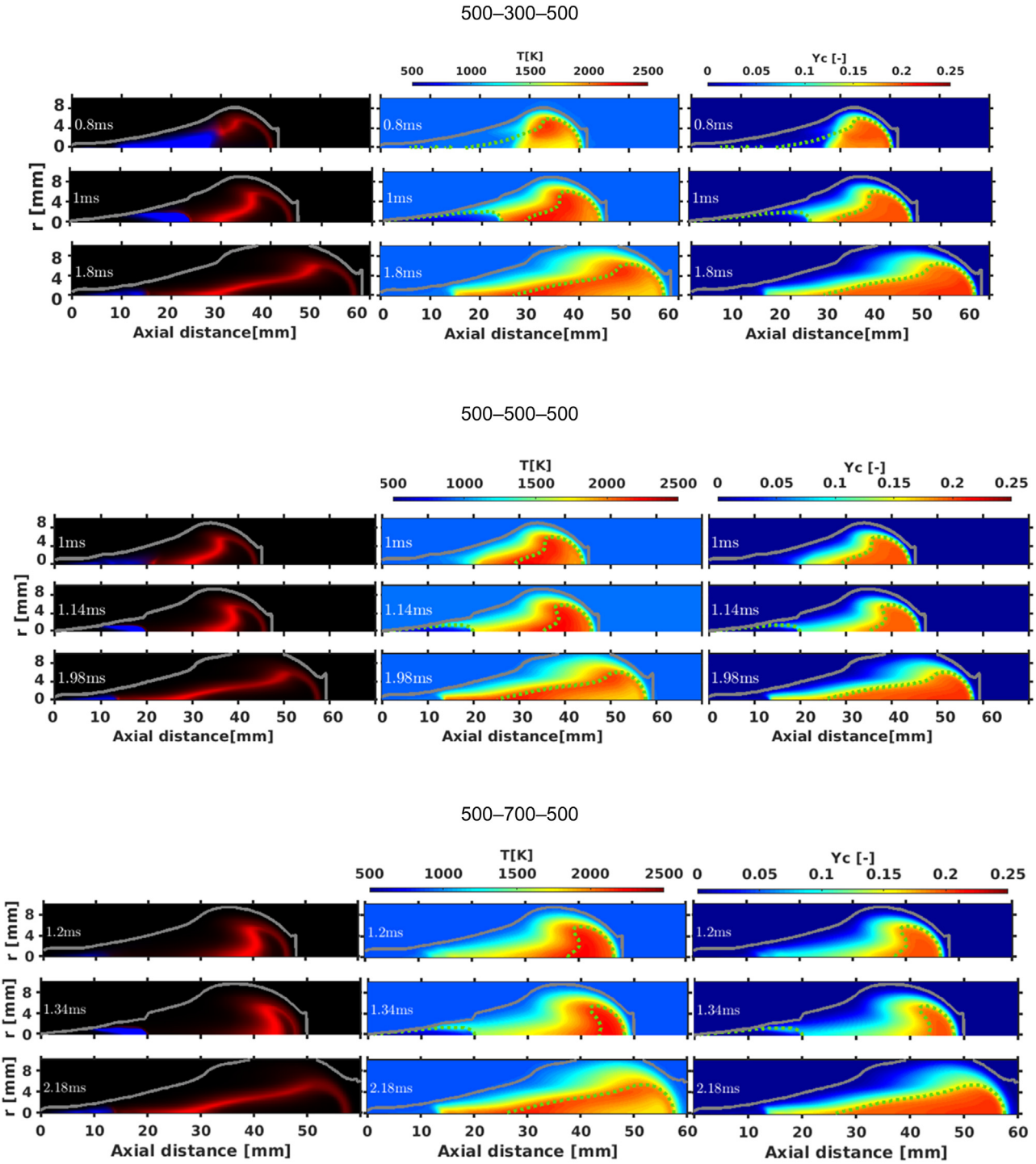

Fig. 8. CFD normalized species mass fractions of OH and CH2O (shown in red and blue, respectively (left)), temperature (middle), and Yc (right) at three characteristic timings (SOI2 (top), ID2 (middle), and maximum soot production (bottom)) for dwell variations. Black solid lines identify spray boundaries, and green dashed lines correspond to stoichiometric surface.

is well captured by CFD. The high-temperature zone is clearly shown on top of the stoichiometric iso-contour in the second injection. However, the soot temperature of the first injection was significantly higher than that of the second injection because more oxygen was entrained into the spray head.

- Finally, the results at 1920 μs ASOI1 show that both pulses had already merged, and the maximum quantity of soot during the injection cycle had been reached. Most of the soot was located at the spray center and close to the spray tip. A combustion recession reappeared after the end of the second injection. Note that the entrainment wave was located at 43 mm (i.e., upstream of the maximum soot cloud).

Figure 5 shows the total soot mass evolution, $m_{soot}(t)$, within the jet versus time. In addition, the corresponding soot temperature averaged over the symmetry plane is presented. Double-peak evolution is observed for the soot mass, consistent with previously described sequences in which soot production starts after the end of the first pulse and drops over time. It is followed by a stronger soot production from the second pulse owing to the injection oc-

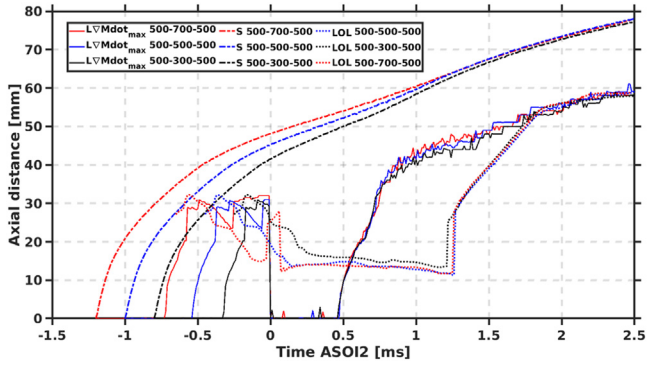

Fig. 9. Time-resolved tip penetration, LOL, and distance to maximum momentum flux gradient for three dwell time cases. Time base shifted to start of second injection (ASOI2).

curring in a high-temperature area where combustion products are present. Maximum soot values are reached at the time when oxidation overcomes formation. Remarkably, both soot peaks were reached at 500 μs (or 1000 μs) after the end (or start) of the corresponding injection pulse; as discussed above, this is related to the time required for the end-of-injection wave to reach the jet tip. Figure 2 shows how the end-of-injection wave propagates downstream from the nozzle for both pulses. Note that the simple metrics applied for this analysis do not fully capture the final interaction between the wave and tip of the jet. However, trends confirm that soot reaches a peak when this interaction occurs, providing additional entrainment that enhances soot oxidation. Moreover, the oxidation of the rich spray tip head consistently coincides with an increase in the overall temperature, as shown in the corresponding plot. Both experimental and numerical results indicate a strong relationship in timing and evolution between the end-of-injection event and the transient combustion and soot production.

A similar trend in quantitative terms can be found between the experimental and CFD results; the amount of soot generated is 80% higher, and the average temperature is reduced by approximately 13%. The current CFD setup was already found to overpredict the accumulated soot mass for long injection cases [29,41]. The results for the highly transient conditions in this work show that the oxidation phase is considerably less prominent than those in the experiments, leading to higher soot production and prolonged soot existence. However, the timing of relevant events is considerably similar to that in the experiments, with peak soot production occurring slightly later than 1000 μs (ASOI2).

In summary, considering both the spatially resolved (Fig. 4) and integrated (Fig. 5) soot masses, the CFD predictions are in reasonable agreement with the experimental data in terms of events and locations describing combustion and soot production. Consequently, they are used to analyze the variations in dwell time and duration of the first injection, as presented in the following sections.

5.2. Effect of dwell time

To analyze the effect of dwell variations on the soot characteristics from the second injection, the total soot mass evolution, $m_{soot}(t)$, and the corresponding average soot temperature are presented for the three different dwell time cases in Fig. 6. The time base is shifted such that it is referenced to the start of the second injection (ASOI2) to enable a clearer evaluation of the second injection processes. Because the first-injection pulse was the same, identical soot formation and average temperature values were obtained for all the three cases along the first pulse. For the nominal case (500–500–500), the first soot onset starts at 750 μs ASOI1, followed by an increase in soot mass until a peak at 1000 μs ASOI1 is reached; this corresponds to the start of the second injection. Subsequently, soot oxidation becomes the governing process; hence, the total soot mass decreases. For the other cases, the previous timings are simply shifted when converted to the reference at the start of the second injection, resulting in the distribution shown in the plot.

For the second pulse, no sign of soot formation is observed until approximately 500 μs ASOI2 (all three cases are relatively coincident at this time). This means that similar to the first pulse, the soot increase due to the second pulse also occurs after the end of injection. A sharp increase until a peak value is reached at 1000 μs ASOI2 is observed; then, the oxidation processes become dominant. The dwell time of the injection pulses had no effect on the soot peak timing and only has a relatively minor effect on the amount of soot produced by the second pulse. Hence, the soot increase in the second pulse is identical for the 300 μs and 500 μs dwell time cases. In contrast, a slightly lower soot peak is observed for the 700 μs dwell time case.

A quantitative description of the overall soot temperature is also shown in Fig. 6. Again, the differences in temperature for the first-injection pulse in this plot are due to the time shift among the different cases. After the initial soot formation, no significant differences were observed in the average soot temperature of the second injection for the three dwell time cases.

An interesting finding from Fig. 6 is that all relevant timings for the second pulse description (specifically the soot onset (approxi-

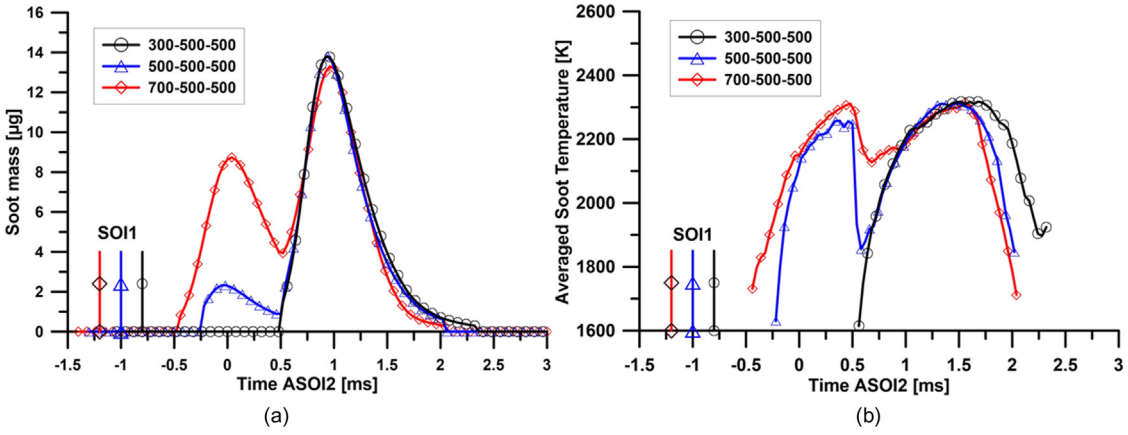

Fig. 10. (a) Temporal evolution of total soot mass and (b) average soot temperature in experiments of different first-injection-duration cases as a function of ASOI2.

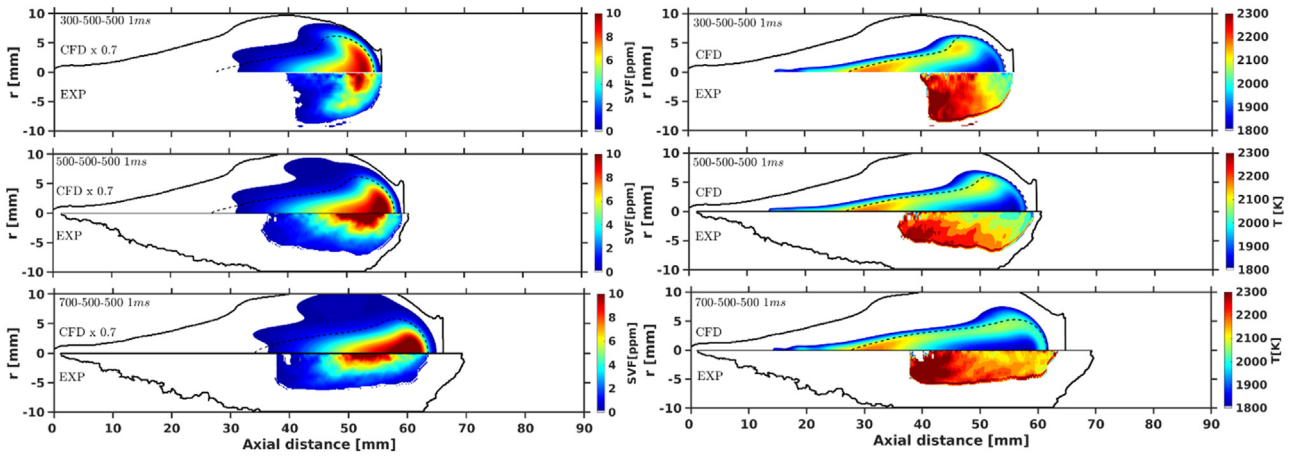

Fig. 11. Experimental (bottom half-plane) and numerical (top half-plane) results of SVF on symmetry plane (left panels) and soot temperature distribution (right panels) at 1000 μs ASOI2 for different first-injection-duration cases: 300–500–500 (top), 500–500–500 (middle), and 700–500–500 (bottom). Black solid lines identify spray boundaries, and dashed lines correspond to stoichiometric surface. To enable comparison between CFD and experimental results with the same color scale, SVF corresponding to CFD is multiplied by 0.7.

mately 500 μs ASOI2), soot peak (approximately 1000 μs ASOI2), and temperature peak (approximately 1500 μs ASOI2)) are similar among the different dwell time cases when referenced to the start of the second injection. This was expected for the soot formation from the first pulse but not for the second pulse.

The distributions of SVF and soot temperature on a symmetry plane for different dwell time cases are shown in Fig. 7 for both experiments and CFD modeling, respectively, at 1000 μs ASOI2 (the characteristic time at which the maximum total soot mass within the flame is observed in the experiments). In the experimental and CFD results, the spray contours exhibit a considerably similar spray tip penetration (approximately 60 mm) for the 500 μs and 700 μs dwell time cases. Although the schlieren images were not recorded for the 300-μs dwell time case, the CFD results showed that the corresponding penetration at 1000 μs ASOI2 was similar to those of the other two cases. The accumulated mass of the three cases is virtually coincident at this instance (Fig. 6); nevertheless, the spatial soot distributions among the different dwell values slightly differ in both experimental and numerical results. The longest dwell time case had a narrow soot distribution along the radial direction, whereas the cases with a shorter dwell time seemed to exhibit a wide soot spread. However, the high-soot and high-temperature areas were similar, resulting in a similar total soot mass and average temperature.

To clarify the relevant combustion processes, CFD-derived data at three characteristic times are presented in Fig. 8 for each of the different dwell times. The first timing corresponds to the start of the second injection, the second one corresponds to ID2 (ignition time of the second injection), and the last one is retrieved at 1000 μs ASOI2 (the time when the mass of the experimental soot approaches its maximum). The left panels in Fig. 8 present color-coded images for the normalized mass fractions of CH_2O and OH in blue and red, respectively. Temperature maps are presented in the middle panels. In the right panels, the spatial distribution of the progress variable ($Y_c = Y_{H_2O} + Y_{CO_2} + 0.75\ Y_{CO}$) is shown to quantify the presence of combustion products (high values indicate the presence of CO_2, CO, and H_2O). The location of the stoichiometric mixture fraction is shown in both the temperature and progress variable plots (green dashed lines).

In all the three cases, the second pulse was injected into the remnants of the combustion zone created by the first injection. In particular, the high ambient temperature region created by the first injection enclosed most of the combustion products. At SOI2, the tip of the jet was distinctly further away from the nozzle with a longer dwell time; however, the combustion recession changed the temperature distribution in the vicinity of the nozzle. For the case of the 500 μs dwell time, both the highest temperature and OH values were found to occur closest to the nozzle, similar to the experimental observations from OH* chemiluminescence. For the longest dwell time, i.e., 700 μs, high temperatures were also reached even at 10–20 mm from the nozzle. In contrast, the high-temperature flame started to move downstream, consistent with the OH mass fraction distribution. Accordingly, a slight variation in ID2 (Appendix A), i.e., 180–112–90 μs, occurs when the dwell time is varied from 300 through 500 to 700 µs. This 90-μs overall variation in ID2 does not seem to produce significant differences in the distribution of species and temperature along the second pulse. This is supported by the virtually identical distribution of temperature and species at ID2 (middle row in Fig. 8) from the nozzle to the tip of the second jet (approximately 20 mm) for the dwell times of 500 and 700 μs. Only for the shortest dwell time was the second pulse observed to penetrate slightly further owing to the longer ID2. The differences among the dwell time cases eventually vanish at 1000 μs ASOI2 (bottom row in Fig. 8).

In addition to the ignition of the second pulse, the end-of-injection transient is a second important parameter affecting the combustion and soot evolution. Figure 9 shows the major metrics from Fig. 2(a) (tip penetration, LOL, and $L_{\nabla \mathrm{Mdot}_{\max}}$) for the three cases. The time base was referenced to ASOI2 such that the main analysis focused on the events occurring during the second pulse injection. The differences at the tip penetration are mainly due to the time base change. They show that the tip of the jet is further away from the nozzle with a longer dwell time. Consistent with the species and temperature observations shown in Fig. 8, the flame recession toward the nozzle occurred during the dwell period, with the LOL reaching the closest location to the nozzle for the longest dwell time. After the start of the second injection and subsequent ignition, the LOL stabilized during and even well after the end of the second injection. The third metric, the position of the end-of-injection wave ($L_{\nabla \mathrm{Mdot}_{\max}}$), is triggered at 500 μs ASOI2 for the three cases (identical second pulse duration). Moreover, the evolution is exactly the same irrespective of the previous history. For all the three cases, a fast initial propagation is observed at the end-of-injection pulse from the nozzle until it reaches approximately 35 mm and then it propagates at the tip penetration speed. As previously discussed, the subsequent evolution of $L_{\nabla \mathrm{Mdot}_{\max}}$ tracks the jet-head vortex location. Despite this limitation, at the maximum soot production time (1000 μs

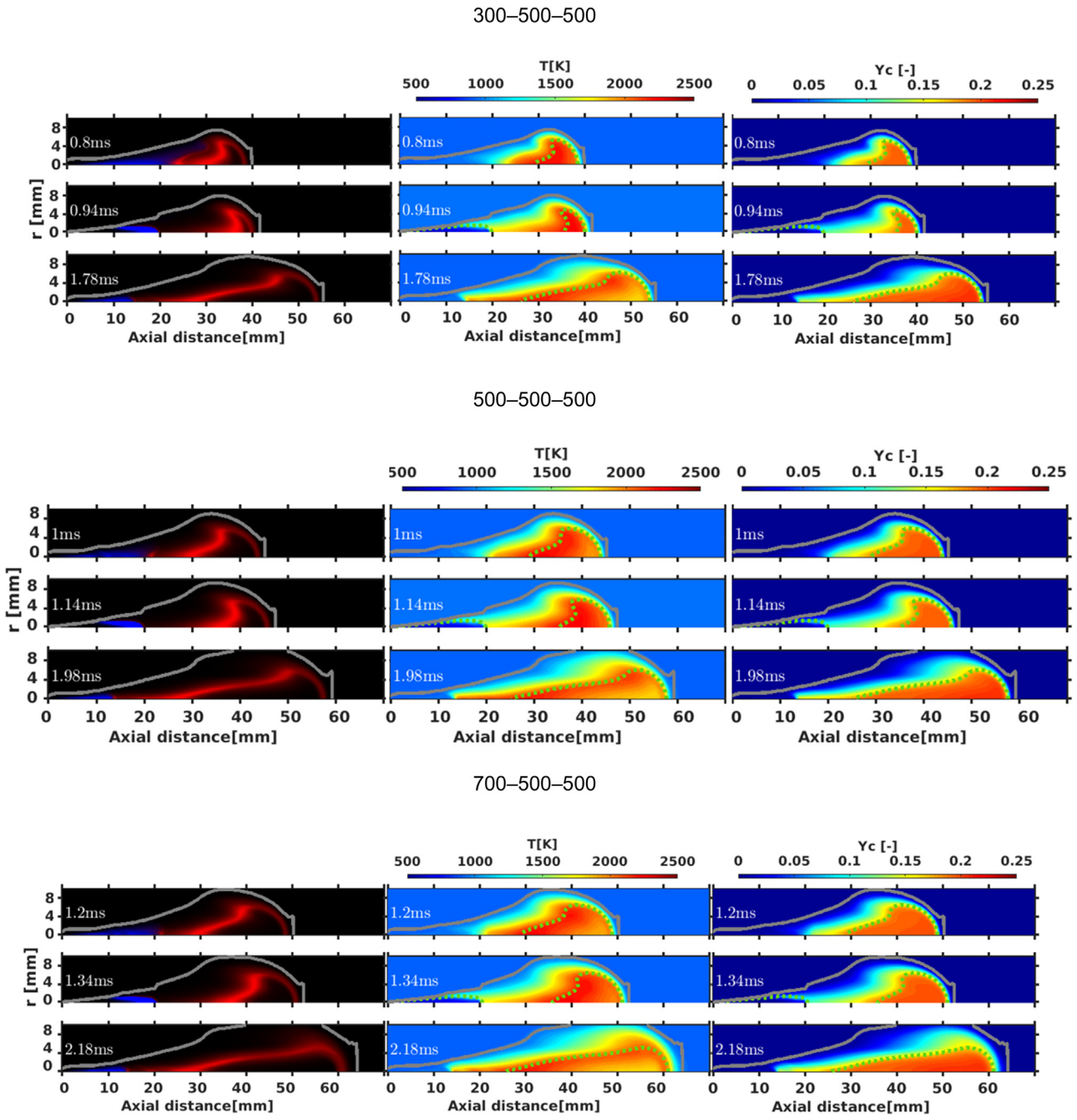

Fig. 12. CFD normalized species of mass fractions of OH and CH2O in red and blue, respectively (left), temperature (middle), and Yc (right) at three characteristic timings (SOI2 (top), ID2 (middle), and maximum soot production (bottom)) for variations in first-injection duration. Black solid lines identify spray boundaries, and green dashed lines correspond to stoichiometric surface.

ASOI2), the end-of-injection wave has reached a position 42 mm away from the nozzle; this is the axial location where soot starts to appear in the spatial distribution shown in Fig. 7. This confirms that the arrival of this wave at the tip zone where soot is present is linked to the maximum soot production. Moreover, the additional entrainment caused by the wave results in a considerable drop in the soot amount within the flame, as indicated by the accumulated soot mass. The propagation of this end-of-injection information does not depend on the dwell time, as indicated by the similar flow states in all the three cases.

In summary, the distributions of species and temperature at the ignition timing of the second pulse are the same for all the three dwell time cases. The subsequent evolution of the second jet along the injection is virtually coincident; this also applies to soot formation. After the end of injection, the transient wave causes further entrainment into the formed soot cloud, considerably governing the soot peak. Because this wave is fundamentally the same for the three dwell time cases, the timing and amount of soot do not change substantially, as shown by the experiments.

5.3. Effect of first injection duration

The same layout as in Fig. 6 is shown in Fig. 10 for the variation in the first injection duration. In this case, significant changes in soot production and temperature in the first pulse can be observed, and the amount of soot increases significantly with the injection

pulse duration. Despite this difference in soot history at the start of the second injection, the experimental results show that the soot onset timing, peak soot value and timing, and average temperature of the second pulse are not extremely sensitive to the first-pulse duration.

Figure 11 shows the corresponding soot and temperature distributions overlaid by spray contours at 1000 μs ASOI2 (maximum experimental soot production) for both experiments and CFD. As shown in Fig. 2, the sooting flame of the second injection initially has a fast penetration rate because of the local low-density ambient created by the first spray flame in the vicinity of the nozzle. Nevertheless, it noticeably decelerates after reaching the spray tip. The case with the longest first pulse (700–500–500) results in a large low-density combustion region into which the second injection proceeded, providing more time for the fast penetration of the second pulse. The SVF and temperature distributions at the time of maximum soot production significantly differ among the three cases. For the shortest first pulse, a wide soot cloud in the radial direction was observed. In the case with the longest first-injection duration, a narrow soot map is observed; this is consistent with the condition in a location further upstream from the spray tip vortex. Despite these differences, the total soot amounts were virtually the same.

Figure 12 shows relevant species, temperature, and progress variable distributions for all the three cases at the same timings similar to the previous dwell time analysis (start of the second injection (SOI2), ID2, and timing of maximum soot production). At SOI2, the species and temperature distributions in the region near the nozzle (0–20 mm in axial extent) are virtually independent from the first injection duration. Even combustion recession has progressed up to the same location (approximately 20 mm from the nozzle for the three cases). This region becomes steady during the first injection due to the top hat injection rate profile. During the dwell period, the end-of-injection entrainment wave also develops in the same manner starting from the nozzle orifice. Hence, differences related to the first pulse can only be observed further downstream near the tip of the spray where most of the mass injected during the first pulse is concentrated.

Owing to the identical conditions in the near-nozzle region into which the second pulse was injected, a virtually identical ID for this second pulse was obtained. This is confirmed by rate of heat release analysis, as presented in Appendix A (where the ID2 values are 124, 112, and 116 μs ASOI2 for the first-pulse durations of 300, 500, and 700 μs, respectively; this is a smaller variation range compared with that found in the dwell study). At ID2, the temperature, species, and progress variable maps in the region where ignition occurs confirm an identical igniting flame distribution. Furthermore, the mass injected during the second pulse was identical in all the three cases (the same injection rate and pulse duration). Consequently, the subsequent combustion development is fundamentally independent of the first pulse mass despite the differences owing to the different tip penetrations downstream of the second jet.

Figure 13 shows the time evolution of the relevant spatial metrics for the analysis of the variation in the first-pulse duration with a time reference at the start of the second injection. The results explicitly show that for the second injection pulse (0–0.5 ms ASOI2), the main differences among the cases occur at the jet tip. In contrast, the flame structure in the nozzle vicinity is the same irrespective of the first-pulse duration (e.g., LOL). This holds true during the dwell time (during which the combustion recession is identical, as shown by the LOL) through the second pulse injection and even after the end of the second injection in which the momentum deceleration pulse evolves in the same way irrespective of the first-pulse duration. Note that for this parametric variation, additional evidence showing that the evolution of $L_{\nabla \mathrm{Mdot}_{\max}}$ when

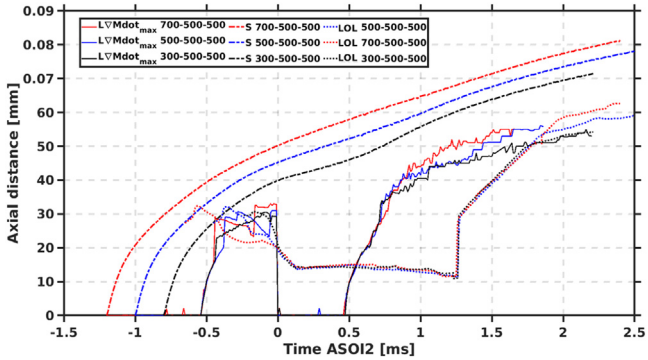

Fig. 13. Time-resolved tip penetration, LOL, and distance to maximum momentum flux gradient for three cases with different first-pulse durations. Time base shifted to ASOI2.

the jet-tip zone is reached (after approximately 40 mm) virtually tracks the jet-head vortex location can be found. In this sense, the slightly longer $L_{\nabla \mathrm{Mdot}_{\max}}$ with a longer first-pulse duration is coincident with the tip penetration trend, despite the virtually identical initial evolution of $L_{\nabla \mathrm{Mdot}_{\max}}$ in all the three cases. At the time of maximum soot production (1000 µs), $L_{\nabla \mathrm{Mdot}_{\max}}$ is located at 40–44 mm, which sets the upstream limit in the high soot distribution shown in Fig. 11. In contrast, the downstream limit is defined by the tip penetration, which varies according to the first-pulse duration.

In summary, the observed trend in soot formation for the second pulse results from two factors. First, the identical combustion characteristics of the second pulse (in terms of both ID and flame evolution) are due to a long first pulse creating a quasi-steady state near the nozzle region irrespective of the first-pulse duration. The second effect is the constant second-pulse duration, which creates an end-of-injection wave governing the soot evolution that is independent of the first-pulse duration. Because of the governing role of this entrainment wave on soot formation, this evolution justifies the fact that the subsequent soot formation is identical among the three cases, consistent with Fig. 10.

6. Conclusion

The effects of different split injection strategies on the in-flame soot production of ECN Spray A flames were investigated using high-pressure high-temperature combustion vessels and CFD models. Case studies were conducted under standard constant Spray A ambient conditions. High-speed schlieren imaging was applied to detect the spray geometry development, and CER methodology was implemented to quantify the amount of soot and temperature simultaneously. Transient information of the high-temperature flame front of the baseline case (500–500–500) was obtained using high-speed OH* chemiluminescence. Despite the differences in vessels and injectors, consistency among all visualization techniques was observed in the experimental results. To substantiate experimental observations, CFD modeling was performed using a RANS UFPV combustion model with a two-equation soot-in-flamelet approach. The results were compared with temperature and species distributions, and although a quantitative comparison of the local values of soot and temperature showed overpredicted soot production and underpredicted temperature values, the prediction of the overall combustion metrics was satisfactory, and the temporal description of events was accurate. Hence, the modeling results were used for the further analysis of the observed experimental results.

For the baseline condition, the second injection was found to cause ignition in the wake of the preceding pulse flame, where a hot region with low oxygen percentage and combustion products

was found. The combustion recession phenomenon occurred under all the conditions investigated; it was quantified using both temperature and OH concentration in the CFD results. Owing to these local conditions, the soot production of the second-injection pulse exceeded that of the first-injection pulse. The high-soot region was confined to the spray center, whereas the high-temperature region was located at the periphery of the soot cloud. The end-of-injection wave propagation, as quantified from the momentum flux distribution, was found to be a major parameter that governed the timing of maximum soot production through the supply of additional entrainment.

A variation in dwell time under the baseline condition resulted in a considerably slight variation in the ID for the second pulse, in line with the evolution of the combustion recession after the first pulse. Hence, differences in dwell times did not cause significant modifications in the species and temperature distributions of the second pulse at ignition. This situation, together with a similar second-pulse duration and subsequent end-of-injection wave propagation, resulted in a similar combustion evolution of the second pulse; consequently, soot production was virtually identical.

On the other hand, quasi-steady flow and combustion patterns that occurred near the nozzle were obtained irrespective of the first-pulse duration owing to the relatively long flat injection profile, as evidenced by the CFD results. This indicated that during the dwell time, the evolution of the spray in the near-nozzle region was identical among the three first-pulse duration cases. Hence, in the subsequent pulse, the conditions for ignition were extremely similar, and a virtually constant ID was observed among the cases. Again, an identical combustion evolution together with a similar second-injection pulse duration and end-of-injection propagation resulted in identical soot production.

In summary, for the investigated variations in dwell time and first-pulse duration, only minor changes in soot production were identified after the start of the second injection. The relatively long first pulse created conditions in the nozzle vicinity that were extremely similar among the different variations (ID differences for the second pulse are within 90 μs based on modeling). As a result, the ignition and flame evolution of the second pulse were fundamentally the same. Because the second-pulse duration was a constant, the subsequent end-of-injection wave propagation governing the maximum soot production timing was also virtually the same under all experimental conditions.

Declaration of Competing Interest

The authors declare that they have no known competing financial interests or personal relationships that could have appeared to influence the work reported in this paper.

Acknowledgments

This research work has been partially supported by the National Natural Science Foundation of China (51906087) and the Natural Science Foundation of Jiangsu Province (BK20190856).

Appendix A – Iginition delay definition based on heat release rate

One characteristic parameter used to quantify the reacting spray evolution is ID. As an example, the ECN standard uses the time that elapses from the start of injection to the point where the maximum derivative of the maximum temperature in the domain is achieved. In the case of split injection strategies, this typical definition is imprecise owing to the interaction between the first and second ignitions, rendering the quantification of the maximum temperature gradients difficult. Accordingly, an ID definition based on the heat release rate and restricted calculations was used.

Figure 14 shows that robust determining the ID of the second injection is possible because the evolution of the heat release in time presents a clear inflection point that determines the beginning of the second injection combustion without the influence of the first injection. To demonstrate this, simulations of a single pulse identical to the first injection of the split injection cases have been implemented such that the effects of the first combustion event on the second event can be discerned. Table 3 summarizes all the relevant IDs from the numerical study.

To establish a more definite approach for comparing the IDs of the second injection, Fig. 15 shows the rate of heat release for all cases referred to ASOI2. For increases in dwell time, the inflection point marking the ignition of the second pulse occurs earlier. With respect to the variations in first-pulse duration, the second ID was virtually identical among the three cases. Although the dwell time and quantity of the second mass injected are the same for all cases, the heat release rate conforms with the amount of mass injected into the first pulse; the more mass injected into the first pulse, the higher the peak of the heat release rate in the second combustion. This trend can be explained by the fact that at the inflection point determined by ID2, a lower heat release rate is obtained with a shorter first pulse duration, upon which the second pulse energy is overlapped.

Appendix B – Calculation of end-of-injection wave position

One critical point for understanding the combustion evolution under transient injection schemes, such as that proposed here, is the analysis of end-of-injection entrainment waves. Musculus and Kattke [45] were the first to identify the importance of spray deceleration after the end of injection. The spray propagating from the nozzle moves further downstream and creates an additional entrainment wave that governs many phenomena occurring during the late combustion phase. Knox and Genzale [49] also linked this transient fluid dynamic effect on the combustion recession observed under certain operating conditions. The quantification of this effect starts from the mass flux, $\dot{m}(x,t)$, which is defined as

$$\dot{m}(x,t) = \int \rho u dA.$$

This variable was calculated by integrating the mass flux in the axial direction across the entire spray cross-section at a given distance, x, from the nozzle. The entrainment rate, $ER(x,t)$, is defined as the axial derivative of the mass flux:

$$ER(x,t) = \frac{d\dot{m}(x,t)}{dx}.$$

Musculus and Kattke compared the evolution of the entrainment rate after the end of injection with that of a steady injection jet with a spatially constant value. The analysis of the transient evolution after the end of injection shows that the ER increases with the axial coordinate, reaching a peak that is approximately three times that of the steady value. This peak marks the location of the entrainment wave and is a tracer of how the end-of-injection information is transmitted downstream from the nozzle.

For split injection cases, such as those in the present study, the quantification of the entrainment wave is difficult to compare with that of a steady case. To enable a more straightforward quantification of this phenomenon, the momentum flux, which is similar to the mass flux, is chosen:

$$\dot{M}(x,t) = \int \rho u^2 dA.$$

To quantify the end-of-injection wave propagation, the corresponding spatial derivative is used:

$$\nabla\dot{M}(x,t) = \frac{d\dot{M}(x,t)}{dx}.$$

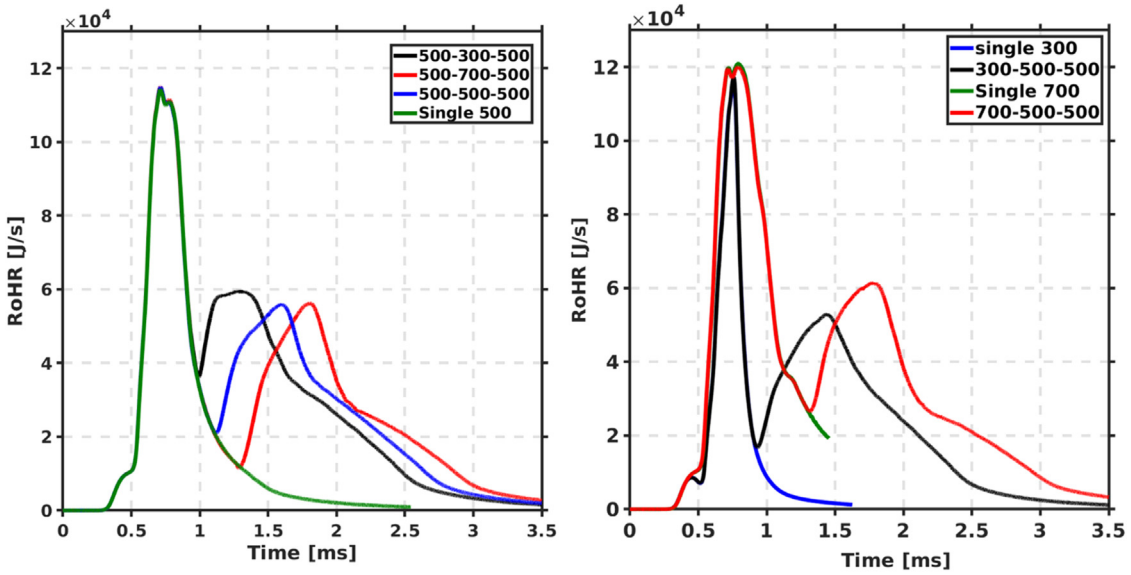

Fig. 14. (a) Rate of heat release for dwell time and (b) second-injection mass variation. Single injection cases at 300, 500, and 700 μs are shown as reference for second-pulse ignition detection.

Table 3
IDs for all calculated cases referred to ASOI1 and ASOI2; nominal case is marked in bold.

	ID1 (ASOI1) [µs]	ID1 (ASOI2) [µs]	ID2 (ASOI1) [µs]	ID2 (ASOI2) [µs]
500-500-500	**543**	**43**	**1112**	**112**
500-300-500	545	45	980	180
500-700-500	545	45	1290	90
300-500-500	557	57	924	124
700-500-500	542	42	1316	116

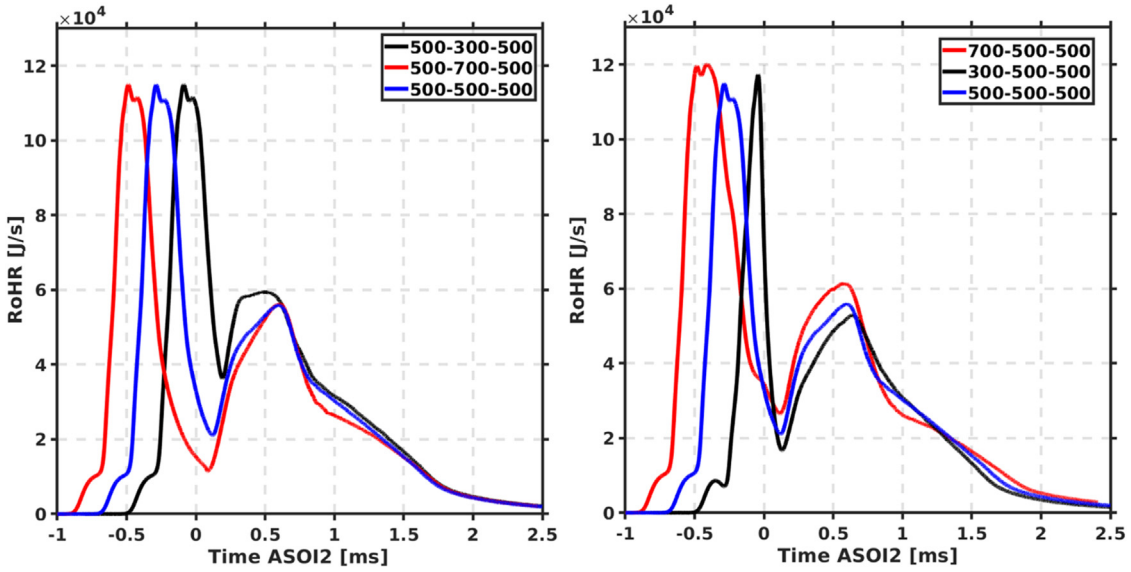

Fig. 15. (a) Rate of heat release for different strategies, variation in dwell time and (b) first-injection duration referred to ASOI2.

The momentum flux for a steady injection rate profile is constant and equal to the nozzle momentum flux (in contrast to the linearly increasing mass flux); therefore, the axial derivative is zero. Starting from this derivative, the position within the spray with the maximum momentum flux gradient, $L_{\nabla \dot{M},max}$, is used to define the most transient location in terms of flow rearrangement after the end of injection.

Figures 16 and 17 show the time evolutions of the mass and momentum fluxes along the spray. Note that both integral quantities are only extended to the gas phase; therefore, they do not contain the entire flow information from the nozzle up to the tip of the liquid length. This results in lower momentum flux values near the nozzle. Moreover, an initially increasing trend in momentum flux corresponding to the exchange between the liquid and gas phases is observed until the maximum liquid length is reached. Further downstream, both the momentum and mass fluxes only correspond to the gas phase.

Starting from the first instant at 0.45 ms, the tip penetration was shown to be approximately 32 mm. The mass flux increased linearly from the nozzle, whereas the momentum flux first in-

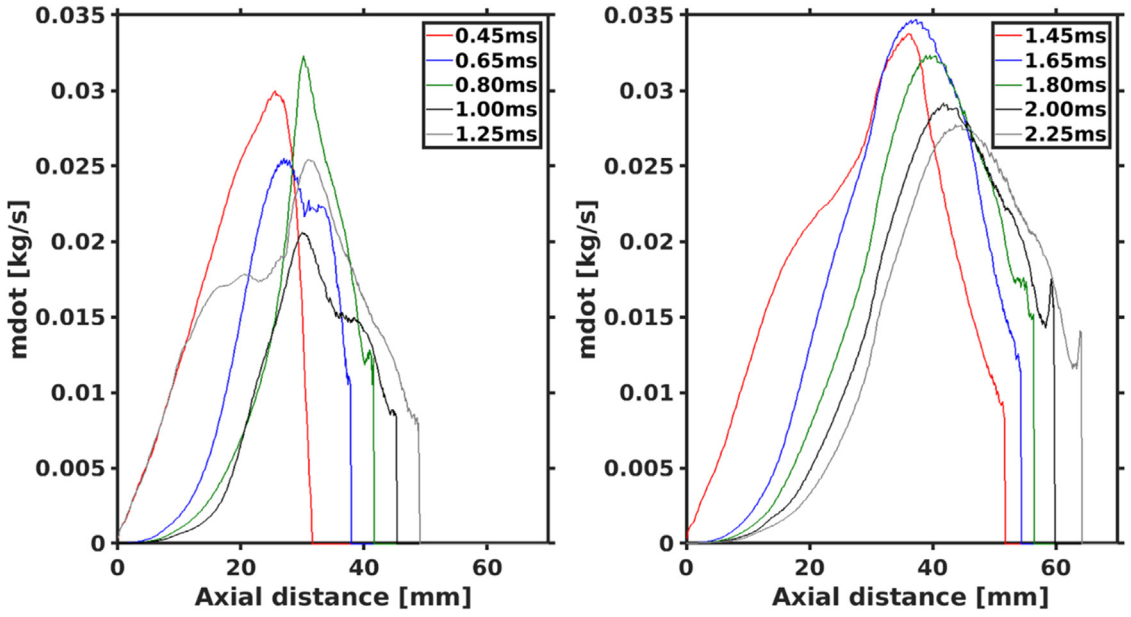

Fig. 16. Time sequence of mass flux along spray axis at different timings in nominal case. For clarity, left plot shows time instants from 0.45 to 1.25 ms; right plot shows those from 1.45 to 2.25 ms.

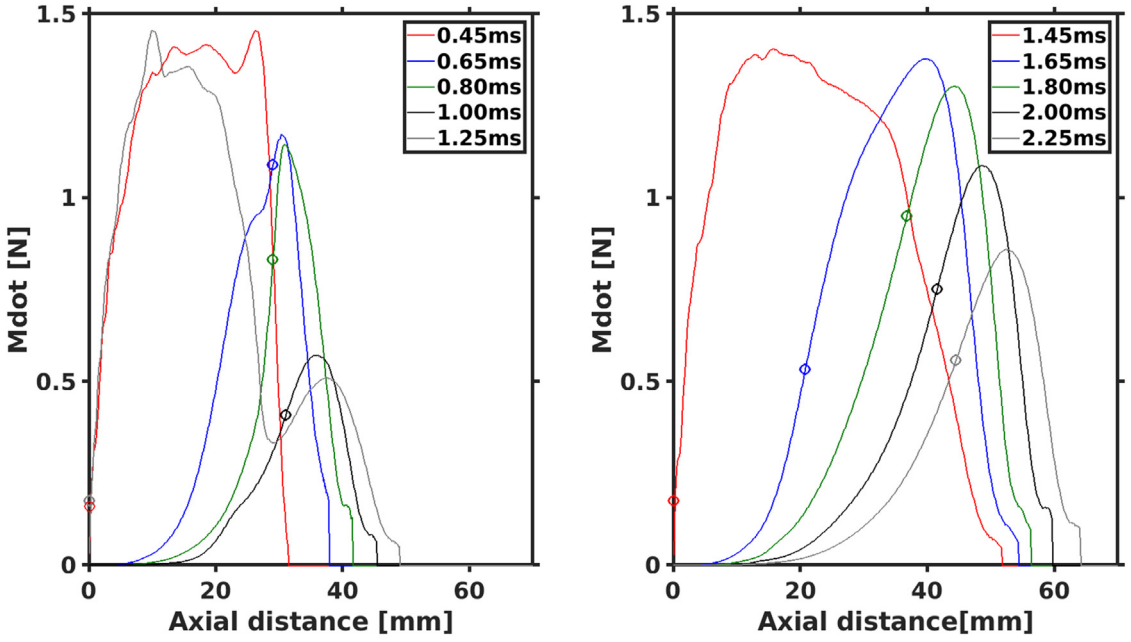

Fig. 17. Time sequence of momentum flux along spray axis at different timings in nominal case. For clarity, left plot shows time instants from 0.45 to 1.25 ms; right plot shows those from 1.45 to 2.25 ms. Markers show positions of $\boldsymbol{L_{\nabla M,max}}$ from the evolution of momentum flux derivative shown in Fig. 18.

creased until 10 mm and remained virtually constant up to the tip of the jet. The liquid length is 10 mm such that only the gas phase information is transmitted further downstream. The quasi-steady nature of the flow is explicitly indicated by the constant momentum flux. The next three instants (0.65, 0.80, and 1.00 ms) cover the dwell time in which both momentum and mass fluxes tend to shift downstream from the nozzle. The axial gradient of the momentum flux (Fig. 18) exhibits a peak value that shifts away from the nozzle. This peak value is defined as $L_{\nabla \dot{M},max}$. At 0.65 ms, two peak values are found on the momentum gradient. The peak value that occurs closest to the nozzle corresponds to the end-of-injection information. The second value is due to ignition, which produces a transient increase in momentum flux. The marker in Fig. 17 shows only the second peak, which has the largest gradient value. The last timing on the left plot shows the results at 1.25 ms; at this instance, the second injection is already underway. The momentum flux reaches a value that is considerably similar to that of the first pulse (0.5 ms) until approximately 30 mm where the second pulse ends; only the remnants of the first injection can be found up to the jet tip. The mass flux is lower than that of the first instant because the presence of hot gas from the previous injection reduces the entrainment. The plots on the right show the time instants immediately before and after the end of the second injection with both mass and momentum fluxes progressively decaying. In this case in which ignition occurred before 1.2 ms, the spray was in a fully reacting state at the end of injection, and the evolution was not disturbed by the ignition process.

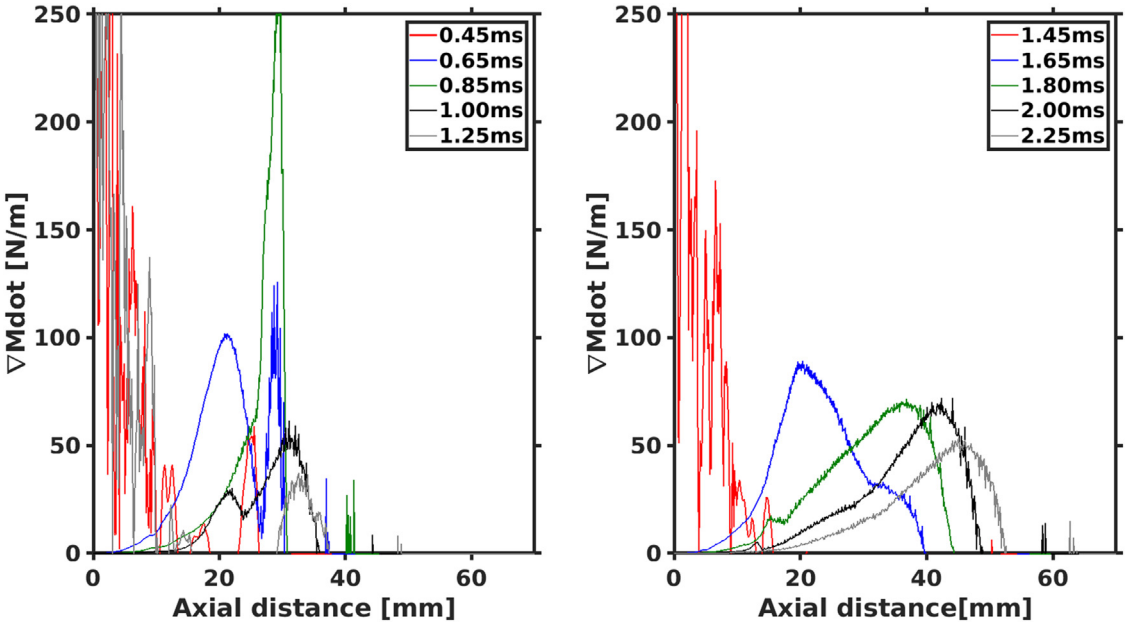

Fig. 18. Time sequence of axial derivative of momentum flux along spray axis at different timings in nominal case. For clarity, left plot shows time instants from 0.45 to 1.25 ms; right plot shows those from 1.45 to 2.25 ms.

References

[1] H.G. How, H.H. Masjuki, M.A. Kalam, et al., Influence of injection timing and split injection strategies on performance, emissions, and combustion characteristics of diesel engine fueled with biodiesel blended fuels, Fuel 213 (2018) 106–114.

[2] D. Babu, R. Karvembu, R. Anand, Impact of split injection strategy on combustion, performance and emissions characteristics of biodiesel fuelled common rail direct injection assisted diesel engine, Energy 165 (2018) 577–592.

[3] D. Kakati, S. Biswas, R. Banerjee, Parametric sensitivity analysis of split injection coupled varying methanol induced reactivity strategies on the exergy efficiency enhancement and emission reductions objectives in a biodiesel fuelled CI engine, Energy 225 (2021) 120204.

[4] S. Breda, F. D'Orrico, F. Berni, et al., Experimental and numerical study on the adoption of split injection strategies to improve air-butanol mixture formation in a DISI optical engine, Fuel 243 (2019) 104–124.

[5] X. Liang, B. Zhao, K. Wang, et al., Impact of multi-injection strategies on morphology, nanostructure and oxidation reactivity of diesel soot particles, Combust. Flame 237 (2022) 111854.

[6] J. O'Connor, M. Musculus, In-cylinder mechanisms of soot reduction by close–coupled post-injections as revealed by imaging of soot luminosity and planar laser-induced soot incandescence in a heavy-duty diesel engine, SAE Int. J. Engines 7 (2014) 673–693.

[7] J. O'Connor, M. Musculus, Effect of load on close-coupled post-injection efficacy for soot reduction in an optical heavy-duty diesel research engine, J. Eng. Gas Turbines Power 136 (10) (2014) 101509.

[8] J. O'Connor, M. Musculus, Post injections for soot reduction in diesel engines: a review of current understanding, SAE Int. J. Engines 6 (2013) 400–421.

[9] S. Skeen, J. Manin, L.M. Pickett, Visualization of ignition processes in high-pressure sprays with multiple injections of n-dodecane, SAE Int. J. Engines 8 (2015) 696–715.

[10] N. Maes, P.C. Bakker, N. Dam, et al., Transient flame development in a constant-volume vessel using a split-scheme injection strategy, SAE Int. J. Fuels Lubr. 10 (2017) 318–327.

[11] A. Hadadpour, M. Jangi, K.M. Pang, et al., The role of a split injection strategy in the mixture formation and combustion of diesel spray: a large-eddy simulation, Proc. Combust. Inst. 37 (2019) 4709–4716.

[12] M. Bolla, M.A. Chishty, E.R. Hawkes, et al., Modeling combustion under engine combustion network Spray A conditions with multiple injections using the transported probability density function method, Int. J. Engine Res. 18 (2017) 6–14.

[13] W. Zhao, H. Wei, L. Zhou, LES study on the interaction between the local flow and flame structure in multi-injection of n-dodecane, Fuel 285 (2021) 119214.

[14] M.P.B. Musculus, K. Kattke, Entrainment waves in diesel jets, SAE Int. J. Engines 2 (2009) 1170–1193.

[15] D. Shin, E.S. Richardson, Mixing Dynamics and Scalar Dissipation Rate in Split-Injection Gaseous Jets, Proceeding of the European Combustion Meeting in, 2015.

[16] D. Shin, E. Richardson, Mixing dynamics and fluid residence time in split-injection gaseous jets, Proceeding of the International Symposium on Turbulence and Shear Flow Phenomena in, 2015.

[17] X. Wen, M. Rieth, W. Han, et al., Investigation of the ignition processes of a multi-injection flame in a diesel engine environment using the flamelet model, Proc. Combust. Inst. 38 (2021) 5605–5613.

[18] A.A. Moiz, K.D. Cung, S.-.Y. Lee, Ignition, lift-off, and soot formation studies in n-dodecane split injection spray-flames, Int. J. Engine Res. 18 (2017) 1077–1087.

[19] S.A. Skeen, J. Manin, L.M. Pickett, et al., A progress review on soot experiments and modeling in the Engine Combustion Network (ECN), SAE Int. J. Engines 9 (2016) 883–898.

[20] C.K. Blomberg, L. Zeugin, S.S. Pandurangi, et al., Modeling split injections of ECN "Spray A" using a conditional moment closure combustion model with RANS and LES, SAE Int. J. Engines 9 (2016) 2107–2119.

[21] Q. Zhou, T. Lucchini, G. D'Errico, et al., Computational modeling of diesel spray combustion with multiple injections, SAE Int. J. Adv. & Curr. Prac. in Mobility 2 (5) (2020) 2839–2858.

[22] G. Bruneaux, D. Maligne, Study of the mixing and combustion processes of consecutive short double diesel injections, SAE Int. J. Engines 2 (2009) 1151–1169.

[23] K. Cung, A. Moiz, J. Johnson, et al., Spray–combustion interaction mechanism of multiple-injection under diesel engine conditions, Proc. Combust. Inst. 35 (2015) 3061–3068.

[24] W. Zhao, H. Wei, M. Jia, et al., Flame–spray interaction and combustion features in split-injection spray flames under diesel engine-like conditions, Combust. Flame. 210 (2019) 204–221.

[25] T. Brands, T. Huelser, P. Hottenbach, et al., Optical investigation of combusting split-injection diesel sprays under quiescent conditions, SAE Int. J. Engines 6 (2013) 1626–1641.

[26] A.A. Moiz, M.M. Ameen, S.-.Y. Lee, et al., Study of soot production for double injections of N-dodecane in CI engine-like conditions, Combust. Flame 173 (2016) 123–131.

[27] T. Xuan, J.M. Desantes, J.V. Pastor, J.M. Garcia-Oliver, Soot temperature characterization of spray a flames by combined extinction and radiation methodology, Combust. Flame 204 (2019) 290–303.

[28] T. Xuan, N. Maes, J.M. Garcia-Oliver, et al., Soot Characteristics of Diesel Sprays with Different Split-Injection Strategies, Proceeding of the 38th International Symposium on Combustion in, 2021.

[29] L. Pachano, C. Xu, J.M. García-Oliver, et al., A two-equation soot-in-flamelet modeling approach applied under Spray A conditions, Combust. Flame 231 (2021) 111488.

[30] M. Bardi, R. Payri, L.M. Malbec, et al., Engine combustion network: comparison of spray development, vaporization, and combustion in different combustion vessels, Atomization Sprays 22 (10) (2012) 807–842.

[31] M. Bardi, G. Bruneaux, L.M. Malbec, Study of ECN injectors' behavior repeatability with focus on aging effect and soot fluctuations. SAE Technical paper 2016-01-0845 (2016).

[32] R. Payri, J.M. García, T. Xuan, M. Bardi, A study on diesel spray tip penetration and radial expansion under reacting conditions, Appl. Therm. Eng. 90 (2015) 619–629.

[33] N. Maes, M. Meijer, N. Dam. B. Somers, et al., Characterization of Spray A flame structure for parametric variations in ECN constant-volume vessels using chemiluminescence and laser-induced fluorescence, Combust. Flame 174 (2016) 138–151.

[34] J.M. Desantes, J.M. Garcia-Oliver, A. Garcia, T. Xuan, Optical study on characteristics of non-reacting and reacting diesel spray with different strategies of split injection, Int. J. Engine Res. 20 (2019) 606–623.
[35] M. Choi, G. Mulholland, A. Hamins, T. Kashiwagi, Comparisons of the soot volume fraction using gravimetric and light extinction techniques, Combust. Flame 102 (1995) 161–169.
[36] U.O. Koylu, G.M. Faeth, Optical properties of overfire soot in buoyant turbulent diffusion flames at long residence times, J. Heat Transf. 116 (1994) 152–159.
[37] J. Manin, L. Pickett, S.A. Skeen, Two-color diffused back-illumination imaging as a diagnostic for time-resolved soot measurements in reacting sprays, SAE Int. J. Engines 6 (2013) 1908–1921.
[38] T.C. Williams, C. Shaddix, K. Jensen, J. Suo-Anttila, Measurement of the dimensionless extinction coefficient of soot within laminar diffusion flames, Int. J. Heat Mass Transf. 50 (2007) 1616–1630.
[39] S. Skeen, K. Yasutomi, E. Cenker, B. Adamson, et al., Observations of soot optical property characteristics using high-speed, multiple wavelength, extinction imaging in heavy-duty diesel sprays, SAE Technical Paper 2018-01-0233 (2018).
[40] K.J. Richards, P.K. Senecal, E. Pomraning, CONVERGE, 2, Convergent Science, Madison, 2018.
[41] J.M. Desantes, J.M. García-Oliver, R. Novella, L. Pachano, A numerical study of the effect of nozzle diameter on diesel combustion ignition and flame stabilization, Int. J. Engine Res. 19 (2019) (2019) 101–121.
[42] K. Narayanaswamy, P. Pepiot, H. Pitsch, A chemical mechanism for low to high temperature oxidation of N-dodecane as a component of transportation fuel surrogates, Combust. Flame 161 (4) (2014) 866–884.
[43] P. Kundu, M.M. Ameen, C. Xu, U. Unnikrishnan, T. Lu, S. Som, Implementation of detailed chemistry mechanisms in engine simulations, ASME. J. Eng. Gas Turbines Power 141 (2019) 011026.
[44] https://www.cmt.upv.es/#/ecn, (2022)
[45] M. Musculus, K. Kattke, Entrainment waves in diesel jets, SAE Int. J. Engines 2 (2009) 1170–1193.
[46] Maes, N., Dam, N., Somers, B., Lucchini, T. et al., Heavy-duty diesel engine spray combustion processes: experiments and numerical simulations, SAE Technical Paper 2018-01-1689, (2018).
[47] J. Benajes, R. Payri, M. Bardi, P. Martí-Aldaraví, Experimental characterization of diesel ignition and lift-off length using a single-hole ECN injector, Appl. Therm. Eng. 58 (2013) 554–563.
[48] Scott A. Skeen, Julien Manin, Lyle M. Pickett, Simultaneous formaldehyde PLIF and high-speed schlieren imaging for ignition visualizationin high-pressure spray flames, Proc. Combust. Inst. 35 (2015) 3167–3174.
[49] B. W.Knox, C. L.Genzale, Scaling combustion recession after end of injection in diesel sprays, Combust. Flame 177 (2017) 24–36.